ACS APPLIED MATERIALS & INTERFACES

Research Article

www.acsami.org

In situ Growth of Ni_xCo_{100-x} Nanoparticles on Reduced Graphene Oxide Nanosheets and Their Magnetic and Catalytic Properties

Song Bai,[†] Xiaoping Shen,*[,†] Guoxing Zhu,[†] Minzhi Li,[†] Haitao Xi,[‡] and Kangmin Chen[§]

[†]School of Chemistry and Chemical Engineering and [§]School of Materials Science and Engineering, Jiangsu University, Zhenjiang 212013, China

[‡]Key Laboratory of Fine Petrochemical Engineering of Jiangsu Province, Changzhou University, Changzhou 213164, China

Supporting Information

ABSTRACT: Ni_xCo_{100-x} (x = 0, 25, 50, 75, and 100) nanoparticles were uniformly in situ grown on reduced graphene oxide (RGO) nanosheets by a coreduction process for the first time. The as-synthesized products were characterized by X-ray powder diffraction (XRD), energy-dispersive X-ray spectroscopy (EDS), X-ray photoelectron spectroscopy (XPS), inductively coupled plasma optical emission spectrometry (ICP-OES), and transmission electron microscopy (TEM). It was found that RGO nanosheets can effectively prevent the aggregation of Ni_xCo_{100-x} nanoparticles. The size and morphology of the Ni_xCo_{100-x} nanoparticles on RGO nanosheets can be slightly adjusted by changing the Ni:Co atomic ratio. The magnetic properties of the RGO-Ni_xCo_{100-x} composites were investigated at 300 and 1.8 K, respectively. The results reveal that the composites have ferromagnetic characteristics and show composition dependent magnetic properties. In addition, these RGO-Ni_xCo_{100-x} nanocomposites also exhibit enhanced catalytic activities toward the reduction of 4-nitrophenol (4-NP) by $NaBH_4$ as compared with bare Ni_xCo_{100-x} alloy, and the RGO-$Ni_{25}Co_{75}$ shows the highest catalytic activity among the obtained nanocomposites. This general and facile coreduction route can be extended to synthesize other alloy nanostructures on RGO nanosheets with various morphologies and functions, and provides a new opportunity for the application of graphene-based materials.

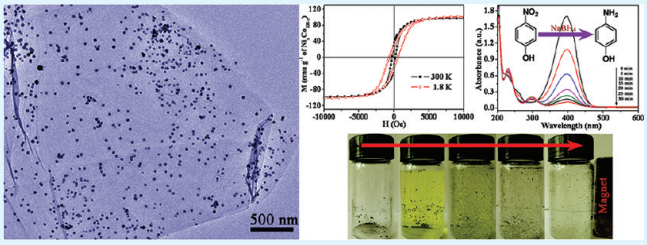

KEYWORDS: *graphene, NiCo alloy, composite, synthesis, magnetic properties, catalytic properties*

1. INTRODUCTION

In recent years, graphene, a monolayer or few layers (<10) of hexagonally arrayed sp^2-bonded carbon atoms, has attracted intense scientific interest mainly because of its large surface area and exceptional electrical, mechanical, thermal, optical, and magnetic properties.[1−5] To date, various synthetic strategies have been developed for producing graphene.[6] Among them, the sonication exfoliation-chemical reduction of graphene oxide (GO) route is both easily scalable, affording the promise for large-scale production, and versatile in realizing abundant chemical functionalization and decoration, benefitting from the residual oxygen-containing functional groups on them.[7] Recently, graphene-based nanocomposites, derived from the decoration of graphene nanosheets with various nanoparticles such as metal, oxide, and sulfide, are emerging as a class of exciting materials that hold promise to broaden the horizons for the use of graphene.[8,9] On the one hand, nanoparticles can act as spacers between graphene nanosheets to minimize the agglomeration of them.[10] On the other hand, the effective integration of nanoparticles with graphene nanosheets can also prevent the aggregation of these active nanoblocks with high surface energy, especially for the magnetic nanoparticles with magnetic interactions.[11] More importantly, the nanocomposites often exhibit enhanced properties and improved functionalities due to the synergetic effects between graphene nanosheets and the nanoparticles, which make them promising application in various fields.[12−15] Nowadays, the integration of graphene nanosheets with magnetic nanoparticles has provided many promising applications in the fields of energy and information storage,[16,17] magnetic resonance imaging,[18] targeted drug carriers,[19] water purification,[20−24] etc. However, these pioneering works about graphene magnetic composite materials are mainly based on the Fe-based compounds.

Ni_xCo_{100-x} alloys represent a class of important transition metal materials, which have been widely used for catalysts,[25] microwave absorption,[26] and magnetic recording media,[27] etc. Nanosized Ni_xCo_{100-x} alloys with different morphologies have been prepared with various method. For example, Ni_xCo_{100-x} nanoparticles, nanowires and nanodumbbells have been successfully synthesized by polyol routes.[28−30] Ni_xCo_{100-x} nanoparticles have also been widely used to combine with other matrix materials, such as polymers, SiO_2, pyrolytic graphite, and carbon nanotubes (CNT) to form nanocomposites for various applications.[31−34] In this paper, we present a facile and general wet chemistry route to grow Ni_xCo_{100-x} (x = 0, 25, 50, 75, and 100) nanoparticles on

Received: November 30, 2011
Accepted: April 10, 2012
Published: April 10, 2012

reduced graphene oxide (RGO) nanosheets for the first time. The influence of the molar ratio of Ni^{2+} and Co^{2+} on the morphology, size and composition of Ni_xCo_{100-x} nanoparticles, and also the magnetic and catalytic properties of the RGO-Ni_xCo_{100-x} composites were systematically investigated.

2. EXPERIMENTAL SECTION

2.1. Materials. Natural flake graphite was purchased from Qingdao Guyu graphite Co., LTD with a particle size of 150 μm. All other chemicals are of analytical grade and used without further purification.

2.2. Preparation of Graphite Oxide. Graphite oxide was synthesized from natural flake graphite by a modified Hummers method.[35] In a typical procedure, 2.0 g of graphite powder was added into cold (0 °C) concentrated H_2SO_4 (100 mL) solution containing $NaNO_3$ (4.0 g) in a 500 mL flask. Under vigorous stirring, $KMnO_4$ (10.0 g) was added gradually and the temperature of the mixture was kept below 10 °C. The reaction mixture was then stirred at 35 °C for 2 h until it became pasty brownish, and was diluted with deionized water (100 mL). The addition of water was performed in an ice bath to keep the temperature below 100 °C. Then, the mixture was stirred for 30 min and 20 mL of 30 wt % H_2O_2 was slowly added to the mixture to reduce the residual $KMnO_4$, after which the color of the mixture changed to brilliant yellow. The mixture was then filtered and washed with 5 wt % HCl aqueous solution (800 mL) to remove metal ions followed by washing with 1.0 L of deionized water to remove the acid. For further purification, the as-obtained graphite oxide was redispersed in deionized water and then was dialyzed for one week to remove residual salts and acids. The resulted solid was centrifuged and dried at 60 °C for 24 h.

2.3. Synthesis of Ni_xCo_{100-x} Nanoparticles on RGO Nanosheets. The typical procedure for the synthesis of RGO-$Ni_{50}Co_{50}$ nanocomposite is as follows: 50.0 mg of graphite oxide, 49.9 mg (0.21 mmol) of $NiCl_2{\cdot}6H_2O$, and 50.0 mg (0.21 mmol) of $CoCl_2{\cdot}6H_2O$ were dispersed in 150 mL of ethylene glycol (EG) with ultrasonication for 1 h ($[Ni^{2+}] + [Co^{2+}]$ = 2.8 mM and molar ratio of Ni:Co = 1:1). Subsequently, under N_2 protection, the obtained yellow dispersion was heated to 110 °C, and 25 mL of hydrazine hydrate dissolved with NaOH (1 g) was slowly added in. The mixture was then refluxed at 110 °C for 45 min. The resultant black product was isolated by centrifugation, washed with water and ethanol, respectively, and finally dried in a vacuum oven at 45 °C. Using the same procedures, Ni_xCo_{100-x} nanoparticles with different composition can be grown on RGO nanosheets by adjusting the molar ratios of Ni^{2+} and Co^{2+} ions. The obtained samples with different metal ion molar ratios were summarized in Table 1. For comparison, pure RGO and bare $Ni_{25}Co_{75}$ alloy nanoparticles were also prepared under the same experimental condition in the absence of the metallic salts and GO, respectively. For the growth of $Fe_{20}Co_{40}Ni_{40}$ alloy nanoparticles on RGO nanosheets, 39.9 mg (0.168 mmol) of $NiCl_2{\cdot}6H_2O$, 40.0 mg (0.168 mmol) of $CoCl_2{\cdot}6H_2O$, as well as 23.4 mg (0.084 mmol) of $FeSO_4{\cdot}7H_2O$ ($[Fe^{2+}] + [Co^{2+}] + [Ni^{2+}]$ = 2.8 mM) were used as metal precursors with all other experimental parameters constant.

Table 1. Samples of RGO-Ni_xCo_{100-x} Nanocomposites Obtained with Different Initial Metal Ion Molar Ratios

samples	initial concentrations of metal ions	Ni^{2+}/Co^{2+} molar ratios
RGO-Co	$[Co^{2+}]$ = 2.8 mM	0:100
RGO-$Ni_{25}Co_{75}$	$[Ni^{2+}] + [Co^{2+}]$ = 2.8 mM	25:75
RGO-$Ni_{50}Co_{50}$	$[Ni^{2+}] + [Co^{2+}]$ = 2.8 mM	50:50
RGO-$Ni_{75}Co_{25}$	$[Ni^{2+}] + [Co^{2+}]$ = 2.8 mM	75:25
RGO-Ni	$[Ni^{2+}]$ = 2.8 mM	100:0

2.4. Characterization. The phase of the as-synthesized products was characterized using X-ray diffraction (XRD, Bruker D8 Advance diffractometer) with Cu Kα radiation (λ = 1.5406 Å) at a scanning rate of 4°·min^{-1}. Raman spectra were carried out at room temperature using a DXR Raman microscope with 514.5 nm excitation source from an Ar^+ laser. The morphology and size of the products were examined by transmission electron microscopy (TEM, JEOL JEM-2100). The compositions of the products were determined by Energy-dispersive X-ray spectrometry (EDS) and inductively coupled plasma optical emission spectrometer (ICP-OES, Vista-MPX). EDS was recorded with an energy-dispersive spectrometer attached to a scanning electron microscope (SEM, JSM-6480). The X-ray photoelectron spectroscopy (XPS) measurements were performed on a PHI 5000 VersaProbe. The magnetic measurements were performed using a Quantum Design MPMS-XL superconducting quantum interference device (SQUID) magnetometer. Ultraviolet−visible (UV−vis) spectroscopy measurements were performed on a UV-2450 UV−vis spectrophotometer.

2.5. Catalytic Reduction of 4-Nitrophenol (4-NP). In a typical reaction, 2.0 mL of 4-NP aqueous solution (5.0 mM) was added into 100 mL of deionized water. Then freshly prepared aqueous solution of $NaBH_4$ (2.0 mL, 1.5 M) was added in, leading to a color change from light yellow to yellow green. Then the as-obtained solution was added into a 250 mL beaker containing 6.0 mg of a catalyst to start the reaction, and the reaction solution was kept stirring. During the reaction process, 2.0 mL of reaction solution was withdrawn at a given time interval, which was immediately recorded in the UV−vis spectrophotometer in a scanning range of 200−600 nm at ambient temperature. For successive recycling of the catalyst in the catalytic reduction of 4-NP, the measured reaction solutions were collected and then mixed with remnant solution in the beaker. The catalysts were magnetically separated from the solution, and then were added into another freshly prepared mixed solution of 4-NP and $NaBH_4$ to start the next round of reaction.

3. RESULTS AND DISCUSSION

3.1. Characterization of RGO-Ni_xCo_{100-x} Nanocomposites. The typical Ni_xCo_{100-x} nanoparticles grown on RGO nanosheets were obtained by simultaneous reduction of Ni^{2+}, Co^{2+} as well as GO in EG medium with hydrazine hydrate and sodium hydroxide as the reductant and pH adjusting agent, respectively. In the sonication process, the graphite oxide were exfoliated in EG to form GO nanosheets. Figure 1a displays digital photographs of vials containing exfoliated GO nanosheets dispersed in EG before and after reduction by hydrazine hydrate. The yellow-brown color of the GO colloid changed to black after reduction, indicating the removal of most oxygen-containing functional groups on GO nanosheets. The XRD patterns (Figure 1b) and Raman spectra (Figure 1c) also confirm the chemical reduction of GO. As shown in Figure 1b, the diffraction pattern of graphite oxide shows a strong peak centered at 2θ = 10.2°, corresponding to its (001) reflection, which disappears in the pattern of the resulting RGO, confirming the good reduction of the GO. Raman spectrum (Figure 1c) of graphite oxide displays two prominent peaks at ca. 1357 and 1605 cm^{-1}, corresponding to the well-documented D and G bands, respectively; while for RGO, the G band moves to ca. 1576 cm^{-1}, close to the value of the pristine graphite, further confirming the reduction of GO.[36] The intensity ratio of the D and G band (I_D/I_G) for RGO shows an enhanced value as compared with that of graphite oxide, indicating more sp^2 domains are formed during the reduction of GO.[37] As usual, the 2D peak at about 2690 cm^{-1} and the D+G peak at about 2930 cm^{-1} for RGO are very weak because of the large number of disorders, which make it difficult to determine the layer number of RGO nanosheets.[4] The obtained RGO nanosheets are larger than several micrometers with wrinkle structure (Figure 1d, e).

The XRD patterns of the as-synthesized RGO-Ni_xCo_{100-x} nanocomposites are shown in Figure 2. The diffraction pattern

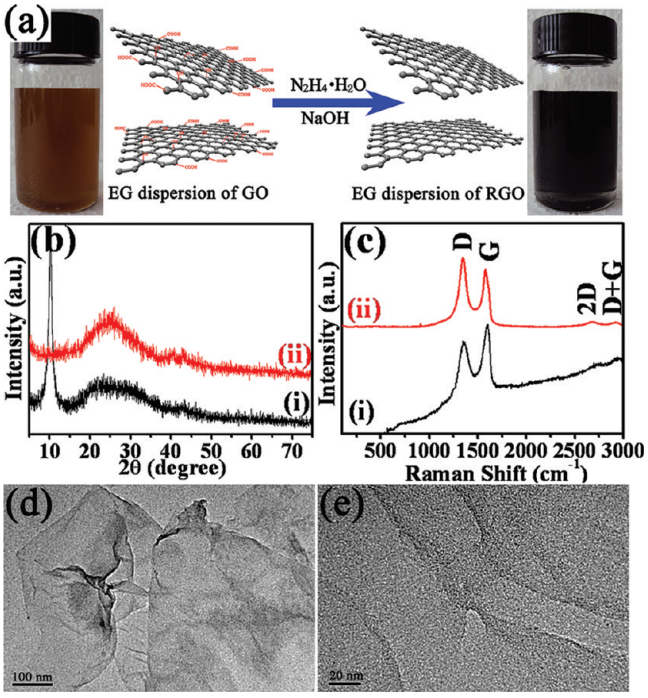

Figure 1. (a) Illustration of the reduction of GO in EG dispersion. (b) XRD and (c) Raman spectra of (i) graphite oxide and (ii) RGO. (d, e) TEM images of RGO nanosheets with different magnifications.

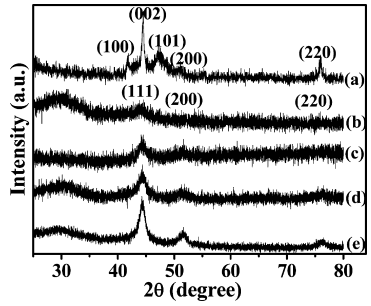

Figure 2. XRD patterns of RGO-Ni_xCo_{100-x} nanocomposites with different molar ratios of Ni^{2+} to Co^{2+}: (a) RGO-Co; (b) RGO-$Ni_{25}Co_{75}$; (c) RGO-$Ni_{50}Co_{50}$; (d) RGO-$Ni_{75}Co_{25}$; and (e) RGO-Ni.

of RGO-Co exhibits peaks at 2θ = 41.8, 44.5, 47.5, 50.9, and 75.9°, corresponding to the (100), (002), (101), (200) and (220) plane of hexagonal close packed (hcp) Co (JCPDS 89–4308). However, the XRD patterns of the other composites show only three peaks, which can be indexed to (111), (200) and (220) planes of a face centered cubic (fcc) structure. The diffraction peaks of RGO-Ni nanocomposites correspond to the fcc Ni (JCPDS 01–1260). The XRD patterns of RGO-Ni_xCo_{100-x} (x = 25, 50, and 75) are very similar to that of Ni (JCPDS 01–1260), with slight variations in peak positions, showing that the introduction of Ni to Co can favor the formation of fcc phase. The (111) peak of RGO-Ni_xCo_{100-x} (x = 25, 50, and 75) lies between the positions of Co (002) and Ni (111) peak, and move toward the position of Co peaks with the increasing Co content, indicating that the lattice constants increase with the increase of Co content. The reason is that the atom radius of Co is slightly bigger than that of Ni, and the substitution of Co for Ni in the Ni-based fcc lattice could result in the increase of cell constants. These results are consistent with the formation of Ni_xCo_{100-x} alloy nanoparticles.[38,39]

However, it is difficult to precisely determine the lattice parameters because the XRD backgrounds are very high due to the presence of a large amount of RGO and the weak crystallinity of the alloy nanoparticles. It is also found that the peak intensity increases with the increase of the Ni content, indicating that higher content of Ni in Ni_xCo_{100-x} will lead to better crystallinity of Ni_xCo_{100-x} nanoparticles.

The high-resolution TEM (HRTEM) image (Figure 3) of a $Ni_{50}Co_{50}$ nanoparticle attached on the RGO nanosheet (Figure

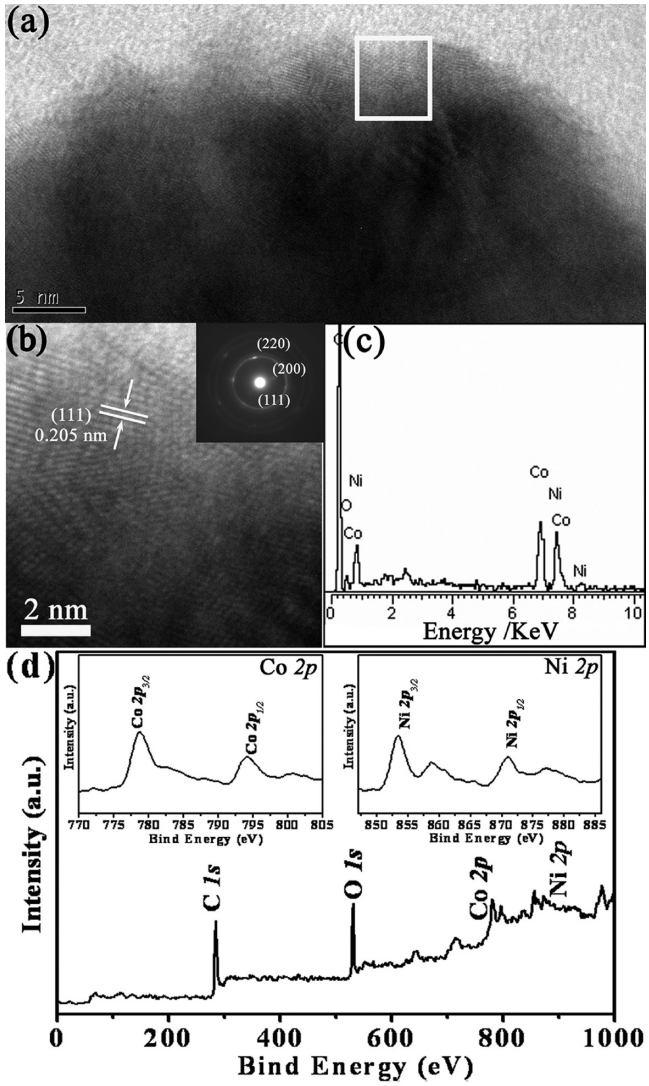

Figure 3. (a) TEM image of the edge of a single $Ni_{50}Co_{50}$ nanoparticle on RGO nanosheet; (b) HRTEM image of the area enclosed by the white box in (a). The inset of (b) gives the corresponding SAED pattern of the selected particle. (c) EDS spectrum of the as-prepared RGO-$Ni_{50}Co_{50}$ nanocomposites. (d) XPS spectrum of the nanocomposites. Insets of d are the XPS spectra of Co 2p and Ni 2p regions, respectively.

3a) reveals the crystalline character of $Ni_{50}Co_{50}$ alloy, and the lattice spacing of 2.05 Å can be indexed to the (111) plane of fcc NiCo crystals.[38,39] The corresponding selected area electron diffraction (SAED) pattern displays a distinguishable ring-like feature, indicating that the as-obtained Ni_xCo_{100-x} nanoparticles are polycrystalline. The EDS spectrum of the as-prepared RGO-$Ni_{50}Co_{50}$ composites was shown in Figure 3c. The detectable elements in the composite include nickel, cobalt,

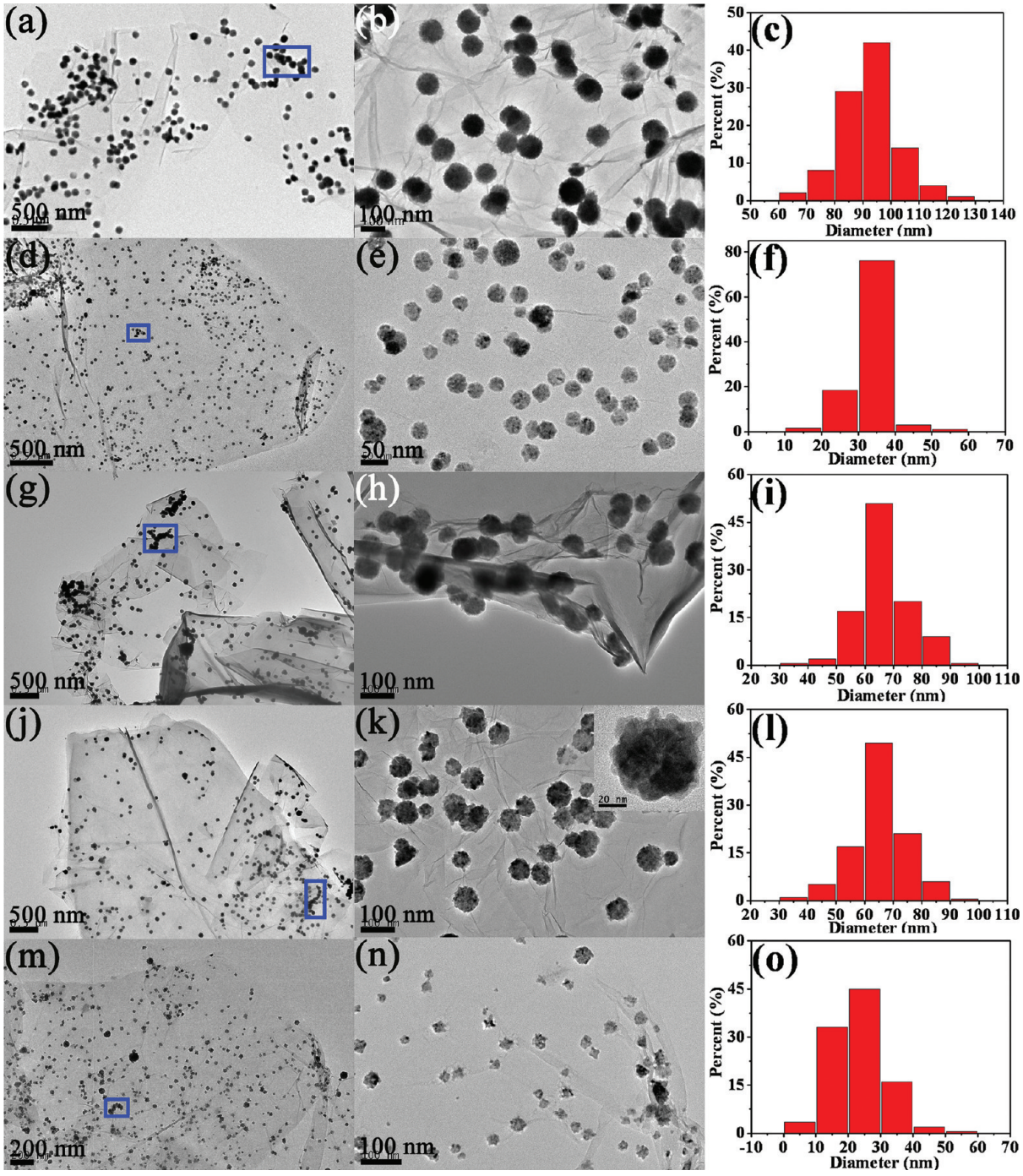

Figure 4. Typical low- and high-magnification TEM images as well as the Ni_xCo_{100-x} particle size distribution of the obtained RGO-Ni_xCo_{100-x} nanocomposites with different molar ratios of Ni/Co: (a–c) Co; (d–f) $Ni_{25}Co_{75}$; (g–i) $Ni_{50}Co_{50}$; (j–l) $Ni_{75}Co_{25}$; and (m–o) Ni. Inset of k is magnified TEM image of an individual $Ni_{75}Co_{25}$ nanoparticle on RGO nanosheet.

carbon and oxygen. The Ni/Co molar ratio obtained from the spectrum was found to be close to the initial 1:1 Ni^{2+}:Co^{2+} molar ratio. The carbon element would come from the RGO nanosheets, while oxygen mainly from the residual oxygen-containing functional groups on RGO. The element composition of the composite were also verified by the XPS spectrum (Figure 3d), which displays the peaks of C 1s (284.8 eV), O 1s (531.2 eV), Ni 2p, and Co 2p. The two obvious peaks at 778.8 and 794.1 eV (inset of Figure 3d) can be attributed to the spin–orbit splitting of Co $2p_{3/2}$ and $2p_{1/2}$, indicating the zero valence of Co, whereas for Ni 2p, the peaks located at 853.2 and 870.9 eV are assigned to the binding energy of Ni $2p_{3/2}$ and Ni $2p_{1/2}$, respectively, which is also agreement with the zero valence of Ni. Both of them reveal the formation of NiCo alloy.[40] The peaks of thin oxide layer inevitable existing on the alloy particle surface are not obvious probably due to the protective effect of RGO nanosheets.[41]

The TEM images of the RGO-Ni_xCo_{100-x} nanocomposites are shown in Figure 4. In all cases, the Ni_xCo_{100-x} nanoparticles are well-dispersed on the surface of RGO nanosheets, although a small amount of nanoparticles tend to assemble into chain-like structure (the area enclosed by the panes), which is a

dx.doi.org/10.1021/am300310d | ACS Appl. Mater. Interfaces 2012, 4, 2378–2386

common phenomenon in the reported pure Ni_xCo_{100-x} nanoparticles because of strong magnetic dipole−dipole interaction.[42−44] This shows that the coreduction process can be generally used in the synthesis of RGO-Ni_xCo_{100-x} nanocomposites, in which the RGO nanosheets with large surface area can prevent the aggregation of Ni_xCo_{100-x} nanoparticles. From the TEM images of the RGO-Ni_xCo_{100-x} nanocomposites with higher magnifications, it can be clearly seen that the Ni_xCo_{100-x} nanoparticles have a narrow size distribution. The detailed particle size distribution of the Ni_xCo_{100-x} nanoparticles on RGO nanosheets are also shown in Figure 4. Among the as-synthesized RGO-Ni_xCo_{100-x} nanocomposites, the pure Co nanoparticles on RGO nanosheets show the largest size (80−100 nm in diameter), whereas pure Ni nanoparticles show the smallest one (10−30 nm in diameter). The average diameters of $Ni_{25}Co_{75}$, $Ni_{50}Co_{50}$, and $Ni_{75}Co_{25}$ nanoparticles are about 33, 67, and 65 nm, respectively. With different Ni−Co composition, the morphologies of the Ni_xCo_{100-x} nanoparticles were also slightly different. The Co nanoparticles exhibit spherical shape structure with smooth surface, while the nanospheres of $Ni_{25}Co_{75}$, $Ni_{50}Co_{50}$, $Ni_{75}Co_{25}$, and Ni with coarse or spinous surfaces. This feature is more obvious with the increasing content of Ni. This may be attributed to the larger susceptibility of Ni, with increasing Ni content, the Ni_xCo_{100-x} nanoparticles will be affected more markedly by the magnetocrystalline anisotropy.[39]

The formation mechanism of the Ni_xCo_{100-x} nanoparticles on RGO nanosheets could be proposed as follows: GO is negatively charged in EG due to the presence of abundant hydroxyl and carboxyl groups. When the metallic salts were mixed with the GO suspension, some Ni^{2+} and Co^{2+} cations would attach to the surface of GO through electrostatic interaction and serve as nucleation sites.[45] When the reductant hydrazine hydrate in alkali solution was introduced, the reduction of Ni^{2+} and Co^{2+} occurred, and primary small Ni_xCo_{100-x} nanocrystallites were formed, while GO nanosheets were also reduced to RGO in the meantime. Then the strong magnetic interaction between the Ni_xCo_{100-x} nanocrystallites promotes them to diffuse and agglomerate into nanoparticles with larger size. The reactions can be expressed as follows[46]

$$Ni^{2+} + Co^{2+} + N_2H_4 + OH^- \rightarrow Ni_xCo_{100-x} + N_2 + H_2O \quad (1)$$

$$GO + N_2H_4 + OH^- \rightarrow RGO + N_2 + H_2O \quad (2)$$

The general coreduction process can also be extended to synthesize other metal and alloy nanoparticles on RGO nanosheets. As a demonstration, the RGO-supported $Fe_{20}Co_{40}Ni_{40}$ ternary alloy nanoparticles were synthesized with simply adding Fe^{2+} into the mixed system (see Figure S1 in the Supporting Information).

The actual chemical composition of the alloy nanoparticles attached on RGO nanosheets was determined by ICP-OES. The contents of Ni_xCo_{100-x} and Ni/Co molar ratio in the composites are given in Table 2. It was found that the actual compositions of these composites are in good agreement with the initial molar ratios of metal ions and their mass ratio with graphite oxide (according to our comparative experiment, 50 mg of graphite oxide can be reduced into about 30 mg of RGO). This indicates that the Ni^{2+} and Co^{2+} are almost quantitatively reduced into metal in the reaction processes.

Table 2. Ni_xCo_{100-x} Content and Ni/Co Molar Ratio of the RGO-Ni_xCo_{100-x} Nanocomposites Determined by ICP-OES

samples	Ni_xCo_{100-x} content (wt %)	Ni/Co molar ratio
RGO-Co	42.5	0:100
RGO-$Ni_{25}Co_{75}$	43.3	25.0:75.0
RGO-$Ni_{50}Co_{50}$	44.1	50.8:49.2
RGO-$Ni_{75}Co_{25}$	43.8	74.1:25.9
RGO-Ni	40.7	100:0

3.2. Magnetic Properties of RGO-Ni_xCo_{100-x} Nanocomposites. The magnetic properties of the as-synthesized RGO-Ni_xCo_{100-x} nanocomposites were measured with a SQUID magnetometer. For quantitative comparison of our data, we normalized the measured magnetization data with respect to the Ni_xCo_{100-x} content of the samples according to the results of ICP-OES. Thus all our magnetization data are given in the unit of emu per gram of Ni_xCo_{100-x}. Figure 5 shows the zero-field-cooled (ZFC) and field-cooled (FC) magnetization curves for RGO-Ni_xCo_{100-x} (x = 25, 50, and 75) nanocomposites measured at 100 Oe. The ZFC curve is measured by cooling the sample down to 1.8 K under a zero magnetic field and then gradually increasing the temperature until 300 K under 100 Oe of magnetic field, and FC curve is recorded in the process of cooling the sample from 300 to 1.8 K under 100 Oe of magnetic field. The ZFC-FC magnetization curves for the three RGO-Ni_xCo_{100-x} composites are much similar, and are not yet superimposed at T = 300 K for all the three samples, showing that these composites are still in the magnetic blocked state at this temperature, which is mainly due to the strong interparticle dipolar magnetic interactions.[47,48]

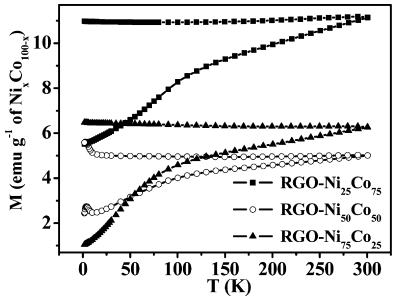

Figure 5. ZFC-FC magnetization curves from 1.8 to 300 K for the RGO-Ni_xCo_{100-x} (x = 25, 50, and 75) nanocomposites under an applied field of 100 Oe.

The hysteresis loops of the RGO-Ni_xCo_{100-x} nanocomposites with different Ni/Co molar ratios are shown in Figure 6, which reveal clearly the ferromagnetic characters of all the synthesized composites. The values of the corresponding magnetic parameters, including saturation magnetization (M_s), remanence (M_r), remanence-to-saturation ratio (M_r/M_s), and coercivity (H_c) are listed in Table 3. The M_s values of Ni_xCo_{100-x} component in the synthesized nanocomposites decrease with the increase of x from 0, 25, 50, 75 to 100, which is consistent with the result reported in bare Ni_xCo_{100-x} nanostructures.[49] For Co and Ni in the RGO nanocomposites, the M_s values are found to be 111.8 and 35.2 emu g^{-1} at T = 300 K, respectively (Figure 6a), which is lower than the reported M_s values of bulk Co (168 emu g^{-1}) and bulk Ni (55 emu g^{-1}).[50,51] This may be attributed to the smaller particle size and the possible presence of the passivating surface layer of

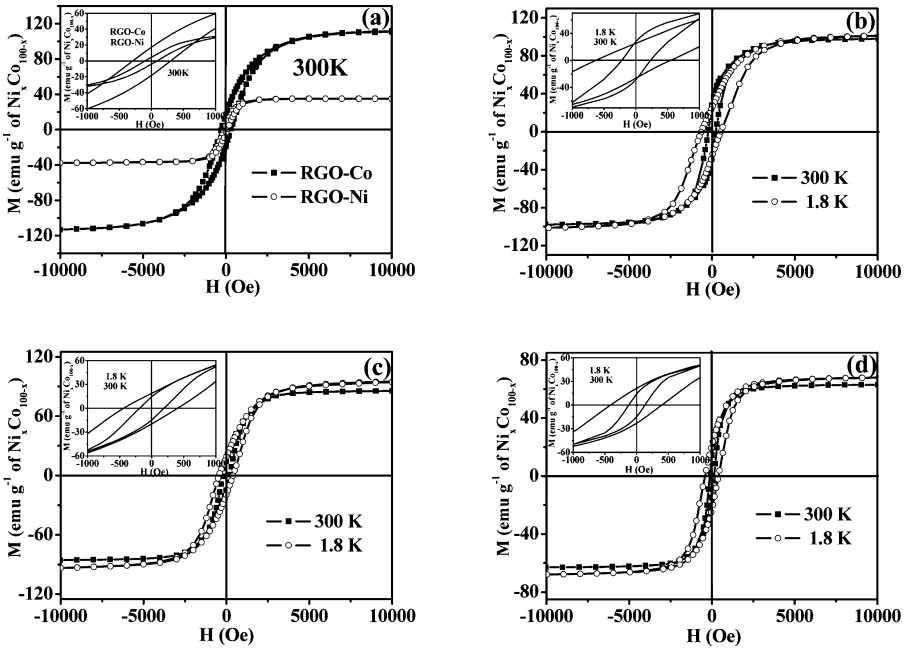

Figure 6. Magnetic hysteresis loops of RGO-Ni_xCo_{100-x} nanocomposites at 1.8 and 300 K: (a) pure Co and Ni (300 K); (b) $Ni_{25}Co_{75}$ (300 and 1.8 K); (c) $Ni_{50}Co_{50}$ (300 and 1.8 K); (d) $Ni_{75}Co_{25}$ (300 and 1.8 K); the inset is magnified hysteresis loops from −1000 to 1000 Oe.

Table 3. Magnetic Data of the RGO-Ni_xCo_{100-x} Nanocomposites

samples	T (K)	M_s (emu g^{-1} Ni_xCo_{100-x})	M_r (emu g^{-1} Ni_xCo_{100-x})	M_r/M_s	H_c (Oe)
RGO-Co	300	111.8	17.2	0.15	292.1
RGO-$Ni_{25}Co_{75}$	300	97.9	28.4	0.29	225.7
	1.8	101.4	24.6	0.24	592.3
RGO-$Ni_{50}Co_{50}$	300	85.6	14.7	0.17	189.8
	1.8	94.8	19.2	0.20	428.5
RGO-$Ni_{75}Co_{25}$	300	63.0	14.6	0.23	125.6
	1.8	68.0	21.9	0.32	401.2
RGO-Ni	300	35.2	4.3	0.12	92.7

metal oxide. The M_s values of the $Ni_{25}Co_{75}$, $Ni_{50}Co_{50}$, and $Ni_{75}Co_{25}$ in the nanocomposites are 97.9, 85.6, and 63.0 emu g^{-1} at 300 K. Although these values are much lower than the value of the bulk $Ni_{20}Co_{80}$ alloy (138 emu g^{-1}),[52] the considerable M_s values make the nanocomposites easily separated from the aqueous dispersion by an external magnetic field (see Figure S2 in the Supporting Information).[53]

The H_c values decrease with the increase of x in the RGO-Ni_xCo_{100-x} nanocomposites. At 300 K, the H_c of Co (292.1 Oe) is higher than that of Ni_xCo_{100-x} alloys (225.7 Oe, 189.8 and 125.6 Oe for $Ni_{25}Co_{75}$, $Ni_{50}Co_{50}$ and $Ni_{75}Co_{25}$, respectively) and Ni (92.7 Oe). This change trend agrees well with other researches on NiCo alloys.[31] The magnetic properties of the RGO-Ni_xCo_{100-x} (x = 25, 50, and 75) composites at T = 1.8 K were also investigated (Figure 6b, c, d and Table 3). The M_s and H_c values at 1.8 K are higher than those at 300 K for all the three samples. Similar to the magnetic data at 300 K, the M_s and H_c values at 1.8 K decrease with the increase of x value. There are no big changes of M_r/M_s at 1.8 and 300 K for these samples, which are lower than 0.35 for all the samples (Table 3). This phenomenon is expected for randomly oriented, blocked nanoparticles.[47,54] The RGO-$Fe_{20}Co_{40}Ni_{40}$ composite also shows similar ferromagnetic behavior but with different magnetic parameters (see Figure S3 in the Supporting Information).

3.3. Catalytic Properties of RGO-Ni_xCo_{100-x} Nanocomposites. The catalytic properties of the RGO-Ni_xCo_{100-x} nanocomposites were quantitatively evaluated with the reduction of 4-NP into 4-aminophenol (4-AP) by $NaBH_4$ as a model system, which was illustrated in Figure S4 in the Supporting Information. This reaction could be easily monitored by the time-dependent UV−vis absorption spectra. As shown in Figure 7, in the absence of the catalysts, the mixture of 4-NP and $NaBH_4$ show a strong peak at 400 nm due to the formation of 4-NP ions under alkaline condition.[55] After the catalysts were added into the system, the absorption peak of 4-NP at 400 nm gradually decreases with the increase of reaction time. Meanwhile, new peaks of 4-AP at 230 and 300 nm appear with their intensity increasing with time, indicating the conversion of 4-NP to 4-AP.[56] It should be noted that the RGO-$Ni_{25}Co_{75}$ shows the highest catalytic activity with about 30 min to finish the reaction (Figure 7b), whereas RGO-$Ni_{50}Co_{50}$ shows the lowest catalytic activity and can not achieve the full reduction of 4-NP even with a reaction time of 200 min (Figure 7c). Compared with RGO-$Ni_{25}Co_{75}$, the catalytic process of bare $Ni_{25}Co_{75}$ nanoparticles is much slower with more than 180 min to finish the reaction (see Figure S5a in the Supporting Information).

It is well-known that the reaction follow the pseudo-first-order kinetics with respect to the concentration of 4-NP when excess $NaBH_4$ was used.[57] In the reaction system, the ratio of C_t to C_0 (C_t/C_0) (C_t and C_0 are 4-NP concentrations at time t and 0, respectively) was measured from the ratio of the absorbances (A_t/A_o) at 400 nm. Good linear correlations (R^2 > 0.97) of $\ln(C_t/C_0)$ versus time t are observed for all nanocomposites, confirming the pseudo-first-order kinetics (Figure 7f, Table 4). Then, the apparent rate constants (k_{app}) were obtained from the slopes of the linearly fitted plots of $\ln(C_t/C_0) - t$, which are provided in Table 4. The k_{app} values show that the catalytic

dx.doi.org/10.1021/am300310d | ACS Appl. Mater. Interfaces 2012, 4, 2378−2386

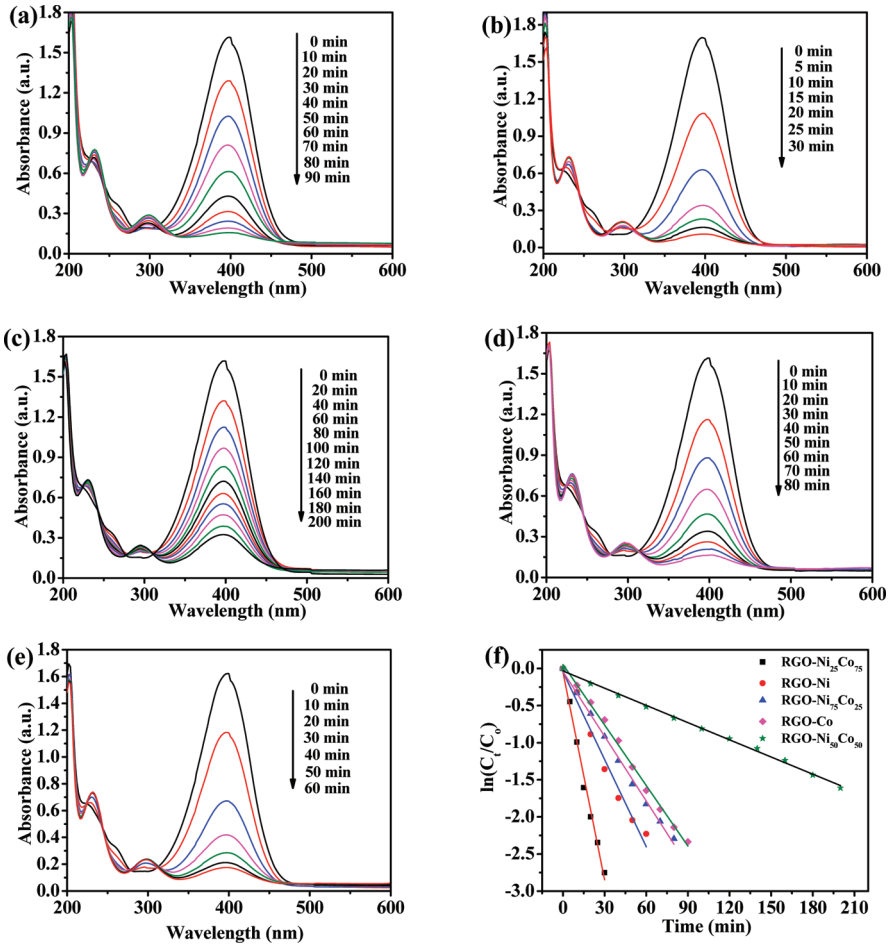

Figure 7. UV−vis absorption spectra of the reduction of 4-NP by $NaBH_4$ in the presence of RGO-Ni_xCo_{100-x} nanocomposites: (a) RGO-Co; (b) RGO-$Ni_{25}Co_{75}$; (c) RGO-$Ni_{50}Co_{50}$; (d) RGO-$Ni_{75}Co_{25}$; (e) RGO-Ni. (f) Plots of $\ln(C_t/C_o)$ of 4-NP versus reaction time for the nanocomposites.

Table 4. Catalytic Rate Constants of the $NaBH_4$ Reduction of 4-NP in the Presence of RGO-Ni_xCo_{100-x} Nanocomposites and the Correlation Coefficient for the $\ln(C_t/C_0)$-t Plots

sample	RGO-Co	RGO-$Ni_{25}Co_{75}$	RGO-$Ni_{50}Co_{50}$	RGO-$Ni_{75}Co_{25}$	RGO-Ni
k_{app} ($\times 10^{-3}$ min^{-1})	27.16 ± 0.60	93.22 ± 3.78	7.73 ± 0.13	29.06 ± 0.60	39.26 ± 2.47
R^2	0.9957	0.9902	0.9973	0.9966	0.9767

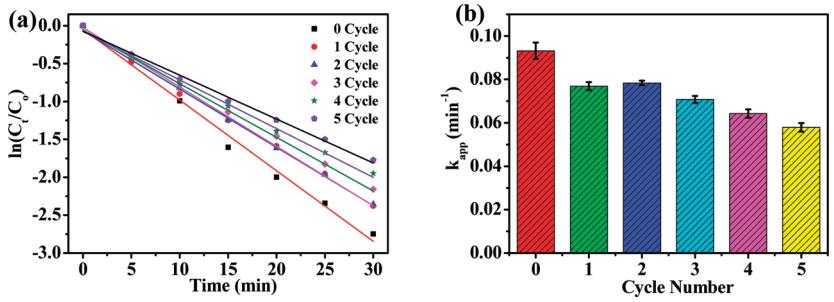

Figure 8. (a) Plots of $\ln(C_t/C_o)$ of 4-NP versus reaction time for successive 5 cycle reactions employing RGO-$Ni_{25}Co_{75}$ composite as catalyst. (b) Value of k_{app} for each cycle with RGO-$Ni_{25}Co_{75}$ composite as catalyst.

activities of RGO-Ni_xCo_{100-x} nanocomposites decrease in the following order: RGO-$Ni_{25}Co_{75}$ > RGO-Ni > RGO-$Ni_{75}Co_{25}$ > RGO-Co > RGO-$Ni_{50}Co_{50}$. The big difference in the catalytic activity is mainly attributed to the different size and composition of the nanocomposites. It seems that the size of metal or alloy nanoparticles plays a main factor for the catalytic activity, thus the samples of RGO-$Ni_{25}Co_{75}$ and RGO-Ni with smaller sizes have higher k_{app} values than others, while the composition is another factor influencing the catalytic activity. It has been demonstrated that the catalytic activity of pure Co is higher than that of pure Ni.[49] Thus RGO-$Ni_{25}Co_{75}$ and RGO-Co show better catalytic performances than RGO-Ni and RGO-$Ni_{50}Co_{50}$, respectively, because of the higher Co contents.

dx.doi.org/10.1021/am300310d | ACS Appl. Mater. Interfaces 2012, 4, 2378−2386

In comparison with bare $Ni_{25}Co_{75}$ nanoparticles (k_{app} = 9.33 × 10^{-3} min^{-1}, see Figure S5b in the Supporting Information), the catalytic activities of RGO-$Ni_{25}Co_{75}$ (k_{app} = 93.22 × 10^{-3} min^{-1}) are much higher (about 10 times of bare $Ni_{25}Co_{75}$), which are comparable to that of noble metal catalyst in the reduction of 4-NP, but the composite is much cheaper, and can be easily separated by a magnet for reuse.[58] The adsorption of 4-NP on RGO via $\pi-\pi$ stacking interaction, the accelerated electron transmission of RGO and the charge transfer between Ni_xCo_{100-x} nanoparticles and RGO were believed to enhance the catalytic activities of the composites in previous literatures.[59,60] The enhancement could also be contributed by the catalytic activity of bare RGO itself, which was found when we compared the UV−vis absorption spectra of the reduction of 4-NP by $NaBH_4$ in the presence of RGO and none of nanomaterials (see Figure S6 in the Supporting Information).[61]

The representative sample of RGO-$Ni_{25}Co_{75}$ was also tested for reusability in the reduction of 4-NP by $NaBH_4$. The magnetically separated catalyst was reused to carry out the reduction process for an additional five times (see Figure S7 in the Supporting Information). After the completion of five cycles, the values of k_{app} for each round of catalytic reaction were obtained from the plots of $\ln(C_t/C_0) - t$ (Figure 8a). The k_{app} for the successive six cycles was shown in Figure 8b, there is only a slight decrease in the k_{app} value with the increasing cycle. In contrast, the k_{app} for bare $Ni_{25}Co_{75}$ nanoparticles drops rapidly in the second cycle process (see Figure S8 in the Supporting Information). These experimental results exhibit that the RGO nanosheets effectively improve the stability of the Ni_xCo_{100-x} catalysts. On the one hand, the RGO nanosheets as support material could protect the Ni_xCo_{100-x} nanocatalysts from aggregation and prevent the framework of the nanocomposites from damage, thus the high stability of the composite structures results in the high stability of the catalytic activity. On the other hand, the high adsorption of the reaction product, 4-AP, on RGO nanosheets can effectively inhibit the poisoning process of the Ni_xCo_{100-x} catalysts, which mainly results from the coverage of 4-AP on the surface of the catalysts.[62]

4. CONCLUSIONS

In summary, RGO-supported Ni_xCo_{100-x} (x = 0, 25, 50, 75 and 100) nanoparticles were successfully synthesized through a coreduction process. It was found that with different Ni−Co compositions, the Ni_xCo_{100-x} nanoparticles with different size and morphology were uniformly grown on RGO nanosheets. The final compositions of Ni_xCo_{100-x} alloys and their contents in the composites match well with the initial feed ratios of the raw materials, which makes the synthesis well-controlled. The formation mechanism of the Ni_xCo_{100-x} nanoparticles on RGO nanosheets was proposed. The simple coreduction process was also extended to synthesize more complex graphene-based nanocomposites such as RGO-$Fe_{20}Co_{40}Ni_{40}$ composite. These RGO-Ni_xCo_{100-x} nanocomposites show ferromagnetic behavior and exhibit excellent catalytic activities and stabilities toward the reduction of 4-NP. It is believed that the obtained nanocomposites have promising applications in catalysis.

■ ASSOCIATED CONTENT

Supporting Information

Figure S1−Figure S8 (PDF). This material is available free of charge via the Internet at http://pubs.acs.org/.

■ AUTHOR INFORMATION

Corresponding Author

*Fax: (+86)511-88791800. Tel: (+86)511-88791800. E-mail: xiaopingshen@163.com.

Notes

The authors declare no competing financial interest.

■ ACKNOWLEDGMENTS

The authors are grateful for financial support from the National Natural Science Foundation of China (51072071 and 51102117) and Key Laboratory Foundation of Fine Petrochemical Engineering of Jiangsu Province (KF0905).

■ REFERENCES

(1) Geim, A. K.; Novoselov, K. S. *Nat. Mater.* **2007**, *6*, 183−191.
(2) Li, D.; Kaner, R. B. *Science* **2008**, *320*, 1170−1171.
(3) Allen, M. J.; Tung, V. C.; Kaner, R. B. *Chem. Rev.* **2010**, *110*, 132−145.
(4) Rao, C. N. R.; Sood, A. K.; Subrahmanyam, K. S.; Govindaraj, A. *Angew. Chem., Int. Ed.* **2009**, *48*, 7752−7777.
(5) Zhu, J. H.; Wei, S. Y.; Haldolaarachchige, N.; He, J.; Young, D. P.; Guo, Z. H. *Nanoscale* **2012**, *4*, 152−156.
(6) Wei, D. C.; Liu, Y. Q. *Adv. Mater.* **2010**, *22*, 3225−3241.
(7) Park, S.; Ruoff, R. S. *Nat. Nanotechnol.* **2009**, *4*, 217−224.
(8) Bai, S.; Shen, X. P. *RSC Adv.* **2012**, *2*, 64−98.
(9) Li, Y. F.; Zhu, J. H.; Wei, S. Y.; Ryu, J.; Sun, L. Y.; Guo, Z. H. *Macromol. Chem. Phys.* **2011**, *212*, 1951−1959.
(10) Si, Y. C.; Samulski, E. T. *Chem. Mater.* **2008**, *20*, 6792−6797.
(11) Xu, C.; Wang, X.; Zhu, J. W. *J. Phys. Chem. C* **2008**, *112*, 19841−19845.
(12) Das, B.; Choudhury, B; Gomathi, A; Manna, A. K.; Pati, S. K.; Rao, C. N. R. *ChemPhysChem* **2011**, *12*, 937−943.
(13) Bai, H.; Li, C.; Shi, G. Q. *Adv. Mater.* **2011**, *23*, 1088−1114.
(14) Li, B. J.; Cao, H. Q.; Yin, G. *J. Mater. Chem.* **2011**, *21*, 13765−13768.
(15) Li, B. J.; Cao, H. Q. *J. Mater. Chem.* **2011**, *21*, 3346−3349.
(16) Li, B. J.; Cao, H. Q.; Shao, J; Qu, M. Z.; Warner, J. H. *J. Mater. Chem.* **2011**, *21*, 5069−5075.
(17) Zhu, J. H.; Luo, Z. P.; Wu, S. J.; Haldolaarachchige, N.; Young, D. P.; Wei, S. Y.; Guo, Z. H. *J. Mater. Chem.* **2012**, *22*, 835−844.
(18) He, H. K.; Gao, C. *ACS Appl. Mater. Interfaces* **2010**, *2*, 3201−3210.
(19) Yang, X. Y.; Zhang, X. Y.; Ma, Y. F.; Huang, Y.; Wang, Y. S.; Chen, Y. S. *J. Mater. Chem.* **2009**, *19*, 2710−2714.
(20) Chandra, V.; Park, J.; Chun, Y.; Lee, J. W.; Hwang, I. C.; Kim, K. S. *ACS Nano* **2010**, *4*, 3979−3986.
(21) Ai, L. H.; Zhang, C. Y.; Chen, Z. L. *J. Hazard. Mater.* **2011**, *192*, 1515−1524.
(22) Li, B. J.; Cao, H. Q.; Yin, J. F.; Wu, Y. M. A.; Warner, J. H. *J. Mater. Chem.* **2012**, *22*, 1876−1883.
(23) Xie, G. Q.; Xi, P. X.; Liu, H. Y.; Chen, F. J.; Huang, L.; Shi, Y. J.; Hou, F. P.; Zeng, Z. Z.; Shao, C. W.; Wang, J. *J. Mater. Chem.* **2012**, *22*, 1033−1039.
(24) Zhu, J. H.; Wei, S. Y.; Gu, H. B.; Rapole, S. B.; Wang, Q.; Luo, Z. P.; Haldolaarachchige, N.; Young, D. P.; Guo, Z. H. *Environ. Sci. Technol.* **2012**, *46*, 977−985.
(25) Raula, M.; Rashid, M. H.; Lai, S.; Roy, M.; Mandal, T. K. *ACS Appl. Mater. Interfaces* **2012**, *4*, 878−889.
(26) Kurlyandskaya, G. V.; Bhagat, S. M.; Luna, C.; Vazquez, M. *J. Appl. Phys.* **2006**, *99*, 104308.
(27) Zhang, L.; Bain, J. A.; Zhu, J. G.; Abelmann, L.; Onoue, T. *J. Magn. Magn. Mater.* **2006**, *305*, 16−23.
(28) Toneguzzo, P.; Viau, G.; Acher, O.; Guillet, F.; Bruneton, E.; Fievet-Vincent, F.; Fievet, F. *J. Mater. Sci.* **2000**, *35*, 3767−3784.
(29) Ung, D.; Soumare, Y.; Chakroune, N.; Viau, G.; Vaulay, M. J.; Richard, V.; Fievet, F. *Chem. Mater.* **2007**, *19*, 2084−2094.

(30) Ung, D.; Viau, G.; Ricolleau, C.; Warmont, F.; Gredin, P.; Fievet, F. *Adv. Mater.* **2005**, *17*, 338−344.
(31) Brayner, R.; Vaulay, M. J.; Fievet, F.; Coradin, T. *Chem. Mater.* **2007**, *19*, 1190−1198.
(32) Mattei, G.; Fernandez, C. D.; Mazzoldi, P.; Sada, C.; De, G.; Battaglin, G.; Sangregorio, C.; Gatteschi, D. *Chem. Mater.* **2002**, *14*, 3440−3447.
(33) Zhang, G. X.; Sun, S. H.; Bostetter, M.; Poulin, S.; Sacher, E. *J. Colloid Interface Sci.* **2010**, *350*, 16−21.
(34) Wu, H. Q.; Cao, P. P.; Li, W. T.; Ni, N.; Zhu, L. L.; Zhang, X. J. *J. Alloys Compd.* **2011**, *509*, 1261−1265.
(35) Hummers, W. S.; Offeman, R. E. *J. Am. Chem. Soc.* **1958**, *80*, 1339−1339.
(36) Chen, W. F.; Yan, L. F.; Bangal, P. R. *J. Phys. Chem. C* **2010**, *114*, 19885−19890.
(37) Stankovich, S.; Dikin, D. A.; Piner, R. D.; Kohlhaas, K. A.; Kleinhammes, A.; Jia, Y.; Wu, Y.; Nguyen, S. T.; Ruoff, R. S. *Carbon* **2007**, *45*, 1558−1565.
(38) Wei, X. W.; Zhou, X. M.; Wu, K. L.; Chen, Y. *CrystEngComm* **2011**, *13*, 1328−1332.
(39) Hu, M. J.; Lin, B.; Yu, S. H. *Nano Res.* **2008**, *1*, 303−313.
(40) Cheng, M. Z.; Wen, M.; Zhou, S. Q.; Wu, Q. S.; Sun, B. L. *Inorg. Chem.* **2012**, *51*, 1495−1500.
(41) Law, Y. T.; Dintzer, T.; Zafeiratos, S. *Appl. Surf. Sci.* **2011**, *258*, 1480−1487.
(42) Tripp, S. L.; Dunin-Borkowski, R. E.; Wei, A. *Angew. Chem., Int. Ed.* **2003**, *42*, 5591−5593.
(43) Hu, M. J.; Lu, Y.; Zhang, S.; Guo, S. R.; Lin, B.; Zhang, M.; Yu, S. H. *J. Am. Chem. Soc.* **2008**, *130*, 11606−11607.
(44) Pan, S. L.; An, Z. G.; Zhang, J. J.; Song, G. Z. *Mater. Chem. Phys.* **2010**, *124*, 342−346.
(45) Bai, S; Shen, X. P.; Zhu, G. X.; Xu, Z; Yang, J. *CrystEngComm* **2012**, *14*, 1432−1438.
(46) Zhu, L. P.; Xiao, H. M.; Fu, S. Y. *Eur. J. Inorg. Chem.* **2007**, *25*, 3947−3951.
(47) Casula, M. F.; Concas, G.; Congiu, F.; Corrias, A.; Falqui, A.; Spano, G. *J. Phys. Chem. B* **2005**, *109*, 23888−23895.
(48) Wei, X. W.; Zhu, G. X.; Liu, Y. J.; Ni, Y. H.; Song, Y.; Xu, Z. *Chem. Mater.* **2008**, *20*, 6248−6253.
(49) Rashid, M. H.; Raula, M.; Mandal, T. K. *J. Mater. Chem.* **2011**, *21*, 4904−4917.
(50) Zhu, G. X.; Wei, X. W.; Xia, C. J.; Ye, Y. *Carbon* **2007**, *45*, 1160−1166.
(51) Zhu, G. X.; Wei, X. W.; Jiang, S. *J. Mater. Chem.* **2007**, *17*, 2301−2306.
(52) Chakroune, N.; Viau, G.; Ricolleau, C.; Fievet-Vincent, F.; Fievet, F. *J. Mater. Chem.* **2003**, *13*, 312−318.
(53) Bai, S; Shen, X. P.; Zhong, X; Liu, Y; Zhu, G. X.; Xu, X.; Chen, K. M. *Carbon* **2012**, *50*, 2337−2346.
(54) Lin, C. R.; Yeh, C. L.; Lu, S. Z.; Lyubutin, I. S.; Wang, S. C.; Suzdalev, I. P. *Nanotechnology* **2010**, *21*, 235603.
(55) Praharaj, S.; Nath, S.; Ghosh, S. K.; Kundu, S.; Pal, T. *Langmuir* **2004**, *20*, 9889−9892.
(56) Rashid, M. H.; Bhattacharjee, R. R.; Kotal, A.; Mandal, T. K. *Langmuir* **2006**, *22*, 7141−7143.
(57) Huang, J. F.; Vongehr, S.; Tang, S. C.; Lu, H. M.; Meng, X. K. *J. Phys. Chem. C* **2010**, *114*, 15005−15010.
(58) Wu, K. L.; Wei, X. W.; Zhou, X. M.; Wu, D. H.; Liu, X. W.; Ye, Y.; Wang, Q. *J. Phys. Chem. C* **2011**, *115*, 16268−16274.
(59) Zhang, Y. W.; Liu, S.; Lu, W. B.; Wang, L.; Tian, J. Q.; Sun, X. P. *Catal. Sci. Technol.* **2011**, *1*, 1142−1144.
(60) Ji, Z. Y.; Shen, X. P.; Zhu, G. X.; Zou, H; Yuan, A. H. *J. Mater. Chem.* **2012**, *22*, 3471−3477.
(61) Gao, Y. J.; Ma, D.; Wang, C. L.; Guan, J.; Bao, X. H. *Chem. Commun.* **2011**, *47*, 2432−2434.
(62) Wang, P; Han, L.; Zhu, C. Z.; Zhai, Y. M.; Dong, S. J. *Nano Res.* **2011**, *4*, 1153−1162.